Subseasonal precipitation forecasts of opportunity over central southwest Asia

Melissa L. Breeden[1,2], John R. Albers[1,2], Andrew Hoell[2]

[1]Cooperative Institute for Research in Environmental Sciences, University of Colorado Boulder, Boulder, CO
5 [2] NOAA Physical Sciences Laboratory, Boulder, CO
Correspondence to: Melissa L. Breeden (melissa.breeden@noaa.gov)

Abstract. Subseasonal forecasts of opportunity (SFOs) for precipitation over southwest Asia during January-March at lead times of 3-6 weeks are identified using elevated expected forecast skill from a Linear Inverse Model (LIM), an empirical

10 dynamical model that uses statistical relationships to infer the predictable dynamics of a system. The expected forecast skill from this LIM, which is based on the atmospheric circulation, tropical outgoing longwave radiation and sea surface temperatures, captures the predictability associated with many relevant signals as opposed to just one. Two modes of variability, El Niño-Southern Oscillation (ENSO) and the Madden Julian Oscillation (MJO), which themselves are predictable because of their slow variations, are related to southwest Asia precipitation SFOs. Strong El Niño events, as observed in 1983,

15 1998, and 2016, significantly increase the likelihood by up to threefold of an SFO 3-4 and 5-6 weeks in advance. Strong La Niña events, as observed in 1989, 1999, 2000, also significantly increased the likelihood of an SFO at those same lead times. High amplitude MJO events in phases 2-4 and 6-8 of greater than one standardized departure also significantly increases the likelihood of an SFO 3-4 weeks in advance. Predictable atmospheric circulation patterns preceding anomalously wet periods indicate a role for anomalous tropical convection in the South Pacific convergence zone (SPCZ) region, while suppressed

20 convection is observed preceding predictable dry periods. Anomalous heating in this region is found to distinguish wet and dry periods during both El Niño and La Niña conditions, although the atmospheric circulation response to the heating differs between each ENSO phase.

1 Introduction

Precipitation over central southwest Asia, defined here as 50-80°E, 22-48°N and encompassing Afghanistan, Pakistan, Iran,

25 Turkmenistan, Uzbekistan, Tajikistan, and Kyrgyzstan, occurs mainly during the cold season from November – April and determines the regions subsequent water supply used for agriculture and consumption (Agrawala et al. 2001; Barlow et al. 2006). It is in this context that accurate precipitation predictions are critical, given the effect of water on food security and livelihoods (Famine Early Warning Systems Network, 2022) in this semi-arid region (Barlow et al. 2016). However, precipitation forecasts from dynamical models lack skill by lead times of three weeks over Southwest Asia (de Andrade 2018;

30 Pegion et al. 2019). An alternative endeavor is identifying the smaller subset of forecasts at lead times of three to six weeks that *are* skillful, so-called 'subseasonal forecasts of opportunity' (SFOs; Lang et al. 2020; Mariotti et al. 2020), by forecasting the forecast skill (Kalnay and Dalcher 1987). SFOs can arise from slowly evolving tropical phenomena such as the El Niño-

Southern Oscillation (ENSO; Newman et al. 2003; Johnson et al. 2014; Domeisen et al. 2019; Mariotti et al. 2020; Albers and Newman 2021), and Madden-Julian Oscillation (MJO; Rodney et al. 2013; Johnson et al. 2014; Li and Robertson 2015; Mayer and Barnes 2021), which can force atmospheric circulation patterns to the extratropics through anomalous divergence (e.g., Sardeshmukh and Hoskins 1988).

Precipitation over southwest Asia may be a favorable target variable and location for SFOs, as both ENSO (Barlow et al. 2002; Nazemosodat and Ghasemi 2004; Hoell et al. 2012; Hoell et al. 2014a; Hoell et al. 2014b; Hoell et al. 2015a; Hoell et al. 2015b; Hoell et al. 2017; Hoell et al. 2018a) and the MJO (Barlow et al. 2005; Nazemosodat and Ghaedamini 2010; Hoell et al. 2013; Cannon et al. 2017; Hoell et al. 2018b) can modulate precipitation in this region. Hoell et al. (2018a) considered the sensitivity of southwest Asian precipitation to central Pacific (CP) and eastern Pacific (EP) El Niño and La Niña conditions and found that while both CP and EP El Niño conditions shifted precipitation anomalies towards the upper tercile, a wide range of extreme precipitation outcomes was still possible. CP La Niña events shifted precipitation towards the lower tercile, while EP La Niña events did not significantly shift precipitation in the region. Hoell et al. (2018b) found that, in the five days following MJO phases 2-4 (enhanced eastern Indian ocean convection), negative precipitation anomalies developed as a response to an anomalous upper-level anticyclone and subsidence. Conversely, MJO phases 6-8 (suppressed eastern Indian ocean convection) were associated with anomalous upper level troughing, ascent, and positive precipitation anomalies. However, Cannon et al. (2017) found a nuanced impact of the MJO on extreme western Himalayan snowfall, due to competing influences of the MJO on the dynamic forcing for vertical motion and moisture availability. The convolved impact of ENSO and MJO activity on precipitation in the region is cited as an additional confounding factor that can obscure the nature of the two teleconnections (Schrage et al. 1999; Hoell et al. 2013; Riddle et al. 2013). Objective methods for considering this combined influence, and how it leads to SFOs, are therefore of interest to both better provide real-time subseasonal forecast guidance and to understand sources of predictability.

Based on past success, this study uses a linear inverse model (LIM; Penland and Sardeshmukh 1995), and its associated signal-to-noise metric 'expected skill' (Sardeshmukh 2000; Newman et al. 2003) to anticipate SFOs over Southwest Asia. Albers and Newman (2019) used expected skill to identify SFOs, at the time of forecast, for North Pacific and North Atlantic 500-hPa geopotential height anomalies. They found that periods of elevated expected skill forecast by the LIM identified more skillful forecasts compared to the The European Centre for Medium-Range Weather Forecasts (ECMWF) - Integrated Forecasting System (IFS) and National Center for Environmental Prediction Climate Forecast System Version 2 (NCEP CFSv2) initialized forecast systems, implying that sources of predictability are common among various model types. Albers and Newman (2021) found that North Atlantic Oscillation (NAO) SFOs could be identified in both the LIM and IFS, and were driven by a set of ENSO-related climate modes, reflecting the utility of the LIM in targeting regional phenomena.

Global processes and their unique interactions with local precipitation and temperature ultimately produce SFOs and can be identified by training a LIM on specific regional/large-scale interactions, as demonstrated in Breeden et al. (2022) for North American 2-meter temperature (2mT). Based on these results, here we develop a LIM for subseasonal precipitation over southwest Asia that has been designed in a similar manner. We will show that precipitation SFOs determined using LIM expected skill can successfully be identified for subseasonal precipitation over southwest Asia with a LIM that is regional in precipitation and temperature but large-scale with the inclusion of hemispheric tropical outgoing longwave radiation (OLR) and sea surface temperatures (SSTs) and 200-hPa Northern Hemisphere streamfunction (Ψ_{200}). Another beneficial quality of the LIM is the negligible computational power needed to generate a long record of hindcasts. This study will focus on LIM SFOs and does not evaluate the skill of other models, though past research suggests that forecasts generated elsewise can similarly be more skilful during LIM-identified SFOs (Albers and Newman 2019; Albers and Newman 2020).

The LIM developed for regional precipitation over southwest Asia is used to test the hypothesis that SFOs can be anticipated using theoretical expected skill and are associated with strong ENSO and MJO events. Section 2 introduces the reanalysis and satellite products employed, how the LIM is constructed, and how SFOs are identified using expected skill. Section 3 shows a comparison of this approach to other methods of anticipating periods of elevated forecast skill, and the correspondence between forecasts of opportunity and ENSO and the MJO. Section 4 contextualizes results and proposes next future steps.

2 Data and Methods

2.1 Data

To train the LIM, Ψ_{200}, 2mT, SST, and OLR data from Japanese Meteorological Agency 55-year Reanalysis (JRA-55; Kobayashi et al. 2015) and precipitation from the Climate Hazards InfraRed Precipitation with Stations (CHIRPS; Funk et al. 2015) dataset are used for the period January - March, 1981-2020. Variables and their respective domains are listed in Table 1. To consider how forecast skill and forecasts of opportunity change as a function of ENSO phase, the Niño3.4 index was calculated using SST anomalies averaged from 5°N-5°S, 170°W-120°W (Trenberth, 1997; Trenberth and Stepaniak, 2001). For examining relationships between skill and the MJO, the real-time multivariate MJO (RMM) index, a combined tropical OLR and circulation index that is designed to capture characteristics of the MJO (Wheeler and Hendon 2004), is employed, including RMM amplitude, which measures MJO strength, and each day's associated MJO phase, which tracks MJO location. Finally, based on results in Section 3b, we assess the strength of tropical OLR anomalies in the south Pacific Convergence Zone (SPCZ; box in Fig. 10), defined as 10°S-2.5°N, 140-180°E. The time series of OLR anomalies in this region is considered as a third metric, in addition to Niño3.4 and RMM, that might increase the likelihood of an SFO occurring.

2.2 Linear Inverse Model

A LIM assumes that the evolution of a subset of climate anomalies, defined in the state vector **x**, can be approximated as the sum of a slowly evolving, potentially predictable component and a rapidly-decorrelating, unpredictable component. Here we consider the evolution of the following climate variables (Eq. (1-2); Table 1):

$$\mathbf{x} = \{SST, OLR, \Psi_{200}, 2mT, Precip\} \qquad \{1\}$$

$$\frac{d\mathbf{x}}{dt} = \mathbf{L}\mathbf{x} + \mathbf{F_s} \qquad \{2\} \qquad ,$$

where the dynamic operator **L** represents the predictable component of the evolution, and $\mathbf{F_s}$ represents state-independent white noise forcing that is unpredictable. The LIM employed in this study is created using **L**, designed to capture 'slow and predictable' weekly-timescale variability, as in past studies (Winkler et al. 2001; Newman et al. 2003; Albers and Newman 2019; Breeden et al. 2020). Any predictable processes represented by the variables in **x** are aggregated in the operator **L**, and their net effect on the predictable evolution of the system is leveraged in the LIM (i.e., ENSO/MJO variability). To the extent the key predictable relationships between the LIM variables, whether truly linear or nonlinear, can be estimated linearly through the covariance between model variables (Eq. (3)), they can be represented by **L**. As such, the LIM can include more information than what is retained in models based on the linearized equations of motion that explicitly exclude nonlinear effects.

Consistent with focusing on the predictable, weekly-varying component of the system evolution, the climate anomalies used in the LIM were calculated by removing the 40-year daily climatology and then applying a 7-day mean. Practically, one cannot use anomalies occurring *after* the initialization date to make a forecast, so instead of a centered 7-day mean, the prior 6 days are averaged with the initialization date's anomalies to create the 7-day running mean anomalies. Many variable combinations and regional domains were tested, and the combination used here was found to produce the highest precipitation forecast skill during SFOs over southwest Asia. Since the leading EOFs retained in **x** are not sensitive to small changes in the 2mT and Precip domains selected, LIM forecasts and SFOs are also not sensitive to small changes in the regional domains. Note that information contained in variables that are not included in this LIM, for instance slowly evolving soil moisture, can still be implicitly included in the LIM variables, such as 2mT.

The instantaneous $\mathbb{C}_0$ and 5-day lagged covariance $\mathbb{C}_{\tau_o}$ between the state vector components are used to determine **L**:

$$\mathbf{L} = ln(\mathbb{C}_{\tau_o} * inv(\mathbb{C}_0))/\tau_o \qquad \{3\}$$

As a practical consideration to reduce the dimensionality of $\mathbf{L}$, each variable in $\mathbf{x}$ is truncated using empirical orthogonal function (EOF) analysis, where enough EOFs are retained to capture most of the variance in each variable and region (Table 1). The covariance and lagged covariance are then computed using the principal components that are retained.

A specific training lag τ_o must be selected to compute the lagged covariance. If the system were perfectly linear and forced by white noise, $\mathbf{L}$ would not be sensitive to the training lag, but in practice there are constraints to the range of training lags that are appropriate, which is determined using the 'tau-test' (Penland and Sardeshmukh 1995). For this LIM, a training lag of five days is used, which is consistent with the range of stable training lags for LIMs similar to the one used here (Winkler et al. 2001; Newman et al. 2003; Breeden et al. 2020; Henderson et al. 2020). For further information on the sensitivity of weekly LIMs to training lag and additional parameters, the reader is referred to Section 5 of Winkler et al. 2001.

Similar to output from numerical forecast models, for each initialization and lead time τ, the LIM generates forecasts of the state vector, $\hat{\mathbf{x}}(\tau)$ (Eq. 4; Fig. 1), by propagating the initial conditions $\mathbf{x}(0)$ forward in time. In the LIM, the propagator $\mathbf{G}(\tau)$ is determined from $\mathbf{L}$ by solving the homogeneous component of Eq. (2) (Penland and Sardeshmukh 1995). For this study, forecasts are generated at a daily timestep out to a lead time of 42 days. We note that because the LIM is trained on daily anomalies with a 7-day running mean applied, that the forecasts are also lower-frequency in nature.

$$\hat{\mathbf{x}}(\tau) = \mathbf{x}(0)\exp(\mathbf{L}\tau) = \mathbf{x}(0)\mathbf{G}(\tau) \quad \{4\}$$

LIM forecast skill is assessed using 10-fold cross-validation, done by removing 10% of the data, re-computing $\mathbf{L}$, and generating forecasts for the 10% of initializations that were removed (e.g., Albers and Newman 2019). This process is repeated to generate forecasts for 1981-2020, initialized daily from 1 January – 20 March each year. LIM forecast skill is assessed two ways: using anomaly correlation coefficient (ACC), where the LIM forecast and un-truncated (i.e., full-field) verification precipitation is compared at each grid point, and using the pattern correlation coefficient (PCC), where the LIM forecast and un-truncated verification precipitation are compared at each timestep using the uncentered, cosine-weighted correlation between all grid points over southwest Asia (e.g., Albers and Newman 2019). ACC measures skill over the full period, while preserving geographic information about skill, while PCC measures the average skill over the entire southwest Asian domain but maintains information about how individual forecasts performed. Week two forecasts are the average forecast using forecast lead times 1-7 days, week two forecasts lead times 8-14 days, week three forecasts lead times 15-21 days, week four forecasts 22-28 days, week five forecasts 29-35 days, and week six forecasts 36-42 days. Weeks 3-4 and 5-6 forecasts are determined using the corresponding 14-day averaged forecasts at the corresponding lead times.

2.2.1 Forecasts of Opportunity

160 A common approach to anticipate SFOs is to focus on a specific predictability source, e.g., strong tropical heating associated with ENSO or the MJO. However, many potentially predictable signals may be evolving at any given time, and the constructive or destructive interference between each signal's teleconnections may enhance or degrade the overall predictable forecast signal for variables that we are interested in, e.g., southwest Asian precipitation. Thus, it is more desirable to use a method that considers *all* relevant signals, and their combined influence, to anticipate the overall likelihood of a skillful forecast over the

165 region of interest. Here, following Sardeshmukh et al. (2000), the theoretical expected skill of a perfect, infinite ensemble member forecast, $\rho_\infty(\tau, t)$ (Eq. (5)), is selected to identify SFOs, based on the method's past success. In particular, expected skill is calculated using the pattern correlation version of the LIM signal-to-noise ratio, S^2 (Eq. (6); Newman et al. 2003) evaluated over the southwest Asian domain is calculated at each forecast lead time τ, and each initialization date t. As a result, S^2 and expected skill are a function of time, but not space:

170

$$\rho_\infty(\tau, t) = \frac{S^2(\tau)}{\{[S^2(\tau)+1]S^2(\tau)\}^{.5}} \qquad \{5\}$$

$$S^2(\tau, t) = \frac{tr[F(\tau)]}{tr[E(\tau)]} \qquad \{6\} \qquad .$$

175 S^2 is determined using $\mathbf{F}(\tau, t)$, the forecast signal covariance matrix determined at a given lead time, which indicates the strength of the predictable signal in the forecasts, and $\mathbf{E}(\tau)$, the forecast error covariance matrix which represents lead-dependent, unpredictable 'noise':

$$\mathbf{F}(\tau, t) = <\hat{\mathbf{x}}(t+\tau)\hat{\mathbf{x}}(t+\tau)'> \qquad \{7\}$$

180

$$\mathbf{E}(\tau) = \mathbb{C}\mathbf{0} - \mathbf{G}(\tau)\mathbb{C}\mathbf{0}\mathbf{G}(\tau)' \qquad \{8\}.$$

Where $'$ denotes the matrix transpose. Note that $\mathbf{E}$ is not a function of time, consistent with the assumption of state-independent noise (Eq. (2)), but does vary with forecast lead time τ.

185

We define SFOs as the top 20% of expected skill forecasts, as this subset accurately identifies significantly more skillful forecasts for a range of lead times (Fig. 2). ACC and PCC during these dates are compared to the skill when, instead of expected skill, the top 20% of Niño3.4 amplitude and RMM amplitude are used to identify periods of elevated skill. The skill during these three subsets of forecasts (expected skill, Niño3.4, RMM) is compared to the skill of the remaining 80% of expected skill

190 forecasts, and the 95% confidence level in the skill differences during the three subsets is assessed nonparametrically, using

bootstrapping with replacement. Similar skill differences were found for a range of 10-25% of the forecasts in the SFO group, and 20% was chosen because it provided the greatest number of samples – useful for further separating forecasts by ENSO and MJO phase later – but small enough so that the subset has significantly elevated skill.

2.2.2 Relative Risk

195   A relative risk ratio is used to quantify shifts in the likelihood of an SFO occurring as a function of ENSO, MJO, and SPCZ OLR strength. This is done, for each index, by determining the fraction of SFOs initialized on days with index values of varying amplitude:

$$FRAC = \text{\# SFOs} / \text{\# dates} \quad \{9\}$$

200

For ENSO and SPCZ OLR, changes in SFOs during positive and negative index values of varying threshold are considered, while the RMM is always positive. Instead, we assess changes in SFOs during MJO phases 2-3 or 6-7 and increasing RMM thresholds. To determine the relative risk of an SFO compared to the probability of one occurring on any random day, we divide FRAC calculated for each threshold and index group by 0.2 – since for top 20% of expected skill dates, the chance of
205   one occurring on any date in the forecast period is 0.2:

$$\text{Relative Risk} = FRAC / 0.2 \quad \{10\}$$

As an example, for weeks 3-4 SFOs when Niño3.4 > 1.5, 117 SFOs are found during the 269 days exceeding that threshold,
210   corresponding to FRAC = 0.44 and Relative Risk = 2.2. The robustness of these estimates is evaluated by determining the 95% confidence bounds around the relative risk estimates using bootstrapping with replacement.

3 Results

Section 3.1 shows how expected skill can stratify skillful and unskillful forecasts to identify SFOs and demonstrates how strong ENSO and MJO phases increase the likelihood of an SFO occurring. Section 3.2 reveals how anomalous SPCZ OLR is
215   observed during both wet and dry SFOs, and how predictable patterns during El Niño and La Niña conditions are associated with unique circulation features.

3.1 Identifying Forecasts of Opportunity

The distribution of LIM forecast skill, measured by PCC during the top and bottom 20% of theoretical expected skill forecasts (Eq. (5)), confirms that the high expected skill group successfully identifies more skillful forecasts than the low expected skill
220   group (Fig. 2). Note that for each lead time, the high and low expected skill dates identified are not necessarily the same. For

lead times of weeks 2-4, both the median and 95th percentile values of the PDFs of forecasts initialized on high expected skill dates show statistically significant shifts towards higher PCC, with the greatest skill increases, relative to the bottom 20% group, at the shortest lead time of two weeks (Fig. 2a-c). The distribution of week 2 PCC is also the narrowest for the high expected skill group, a reflection of the more deterministic nature of forecasts at this lead time, particularly during periods of high signal-to-noise ratio (Eq. (6)). As lead time increases, the distribution of skill widens as forecast uncertainty increases, so that by week 5, the medians are indistinguishable between the two PCC distributions. Still, some skillful forecasts remain at week 5 in the high expected skill group, shown by the statistically significant shift in the 95th percentile of PCC.

Subseasonal precipitation skill, evaluated using ACC for weeks 3-4 and 5-6, is low, as discussed in past studies, but increases substantially during high expected skill periods (Figs. 3-4). The LIM 'All Dates' weeks 3-4 skill of .2-.3 ACC exceeds the week 3 skill of most of the S2S models evaluated by de Andrade et al. (2018) for November – March 1999-2009 (compare Fig. 3a to their Fig. 1). Comparing the three approaches to anticipating SFOs – high expected skill, Niño3.4, and RMM – expected skill most successfully anticipates SFOs at both weeks 3-4 and 5-6. The location of maximum skill shifts southeastward from weeks 3-4 to 5-6, with skill also weakening at longer lead times as expected. While there are some regions experiencing a skill increase during the top 20% of Niño3.4 and RMM amplitude dates, the increases are mainly indistinguishable from the skill of the remaining forecasts (Fig. 3c,d, 4c,d). Splitting the Niño3.4 index to consider only strong El Niño or La Niña events indicates that some regions do experience elevated skill during both phases, though in different, localized regions that only cover a limited portion of the region compared to the forecasts identified using expected skill (Figure S1).

Considering PCC during the high expected skill, Niño3.4 and RMM dates confirms that forecasts initialized during periods of high expected skill generally have higher PCC than those identified using Niño3.4 and RMM (Fig. 5). For lead times between weeks 2-4, median PCC shifts statistically significant shifts at the 95% confidence level reflect the increase in skill, as do the increased probability density of forecasts with PCC > 0.5. By week five, the distributions of PCC during high expected skill and high Niño3.4 dates become indistinguishable, consistent with greater similarity in the regions of skill found using Niño3.4 and expected skill at weeks 5-6 (Fig. 4). Overall, the expected skill metric is more effective at anticipating SFOs than Niño3.4 and RMM.

3.1.1 Relating SFOs to Niño3.4 and RMM Indices

The advantage of using high expected skill to anticipate SFOs is that it measures when the combined signal of *all* forcings (e.g., ENSO, MJO) is high relative to unpredictable 'noise'. High expected skill occurs during periods of constructive interference between signals, while low expected skill reflects periods of deconstructive interference (e.g., Farrell 1988; Farrell and Ioannou 1996; Albers and Newman 2019), and such interference is more intermittent than the individual forcing elements (Figs. 6, 8). As such, despite what is shown in Figures 2-4, many high expected skill dates occur during strong ENSO and

MJO events, as indicated by the overlay of SFOs (black dots) with time series of Niño3.4 (Fig. 6) and RMM (Fig. 8). The
255   bottom 20% of expected skill forecasts are also shown in the vertical light gray lines, to contrast the higher-frequency expected
skill with the lower-frequency Niño3.4 and RMM. The correspondence to Niño3.4 is considered first. Both El Niño events of
1983 and 2016 coincided with high expected skill dates at weeks 3-4 and 5-6, though on different dates; conversely, the 1998
event was not associated with any high expected skill dates at weeks 5-6 but was for weeks 3-4. Strong La Niña events, such
as 1999, also reflect periods of high expected skill. Still, there are many high expected skill forecasts initialized with weak
260   Niño3.4 values, as in 2017, since other processes – including ENSO-related heating not captured by Niño3.4 – can produce a
high signal-to-noise ratio. Moreover, some of the lowest expected skill dates occur during strong ENSO events, such as in
2016 for weeks 3-4 at the beginning of February, suggesting other processes may have been destructively interfering with the
ENSO-related component.

265   High Niño3.4 index amplitude during both El Niño and La Niña events leads to increases in the risk of SFO occurrence, though
more strongly during the former than the latter (Fig. 7). There is a greater relative risk for SFOs in weeks 5-6 than weeks 3-4,
suggesting that at longer lead times within the subseasonal forecast period, ENSO conditions are increasingly important for
SFOs. However, it is important to note that skill during these periods is overall lower than weeks 3-4 (Figs. 3-4), which could
be due to the limited capability of ENSO alone to impact predictability, and/or elevated noise. The asymmetric response during
270   El Niño and La Niña conditions may reflect the fact that there are more frequent high amplitude El Niño events than La Niña
events, increasing the number of samples at higher Niño3.4 thresholds. Indeed, Niño3.4 exceeds 1.5°C on 269 days, compared
to 192 days where Niño3.4 is less than -1.5°C. The stronger response during El Niño conditions than La Niña could also be
consistent with Hoell et al. (2018a), who found precipitation shifts during both CP and EP El Niño events but only CP La Niña
events, although future work is needed to better explore these nuances.

275

Discerning a relationship between MJO phases 2-3 and 6-7, the phases that impart known teleconnections to southwest Asian
precipitation (Hoell et al. 2018b), can be more difficult given the more transient nature of the MJO compounded with transient
expected skill (Fig. 8). Only the relationship between the RMM and weeks 3-4 expected skill is considered, as an MJO
teleconnection at 5-6 weeks lead times is not physically plausible (e.g., Tseng et al. 2018). Still, we do find that particularly
280   strong events for phases 2-3 and 6-7 increase the relative risk of weeks 3-4 SFOs, though sampling introduces spread in these
estimates (Fig. 9). Some particularly high-amplitude MJO events, including phases 2-3 in 1985 and 1994 and phases 6-7 in
2005 and 2018, overlap with periods of weeks 3-4 high expected skill, while some weaker amplitude events overlap with some
of the lowest expected skill dates, such as phases 2-3 in late January 2002. Strong RMM phases 6-7, also increase the relative
risk of SFOs, which is elevated at lower RMM thresholds compared to phase 2-3 and does not display the exponential increase
285   at the highest thresholds. These subtle differences in relative risk sensitivity could reflect true differences in the MJO
teleconnection to the region, or could be due to sampling, as there is high uncertainty in the relative risk estimates given the
small number of events observed at such high thresholds.

3.2 Characteristics of Predictable Dry and Wet Initializations

This section compares the composite patterns preceding predictable wet and dry periods 18 days earlier, revealing the role for anomalous heating near the SPCZ. Next, composite wet and dry periods are split by Niño3.4 sign, revealing how different circulation responses during each phase produce like-signed precipitation anomalies over southwest Asia.

3.2.1 All Initializations

First, we consider the patterns preceding anomalously wet and dry periods regardless of ENSO phase, where 'wet' and 'dry' are defined using the top and bottom terciles of southwest Asian precipitation anomalies, respectively. Wet and dry dates that were associated with weeks 3-4 high expected skill dates initialized 18 days earlier, and were also characterized by a PCC > 0, are considered. A lead time of 18 days is chosen because it falls within the weeks 3-4 forecast period and provides the clearest circulation structures, which are similar but weaker at longer lead times (not shown). An 18-day lag is also consistent with the circulation response to tropical diabatic heating anomalies discussed in Jin and Hoskins (1995), which peaked about 15 days after the heating occurred. For these skillful, high expected skill forecasts associated with the development of anomalously wet or dry precipitation anomalies, we consider the composite circulation and heating patterns observed at the time of initialization, or 18 days before the anomalous precipitation is observed.

Figure 10 shows that during weeks 3-4 SFOs initialized before predictable wet and dry periods over southwest Asia, anomalies are roughly equal and opposite in sign. Before dry periods, positive OLR anomalies are located over the western and central tropical Pacific, signifying suppressed convection, while a 200-hPa anticyclone (positive Ψ_{200} anomaly) is located over southwest Asia, consistent with downward vertical motion and suppressed precipitation. Conversely, predictable anomalously wet periods are associated with enhanced anomalous central Pacific convection and a cyclonic Ψ_{200} anomaly over southwest Asia. One feature present during dry initializations is a small but statistically significant negative OLR anomaly in the eastern Indian ocean, which does not have a counterpart during wet initializations. Southwest Asian precipitation is strongly linked to heating variability in this location (Hoell et al. 2012), and the results here suggest that the relationship might be particularly important for anomalously dry periods.

3.2.2 El Niño and La Niña Initializations

Section 3.1 indicated that, while anticipating SFOs based on the Niño3.4 index alone is less successful than expected skill (Figs. 3-4), periods of strong ENSO activity increase the likelihood a forecast of opportunity occurs, particularly during the strongest events (Fig. 7). During either ENSO phase, periods of anomalously high and low precipitation can occur due to transient disturbances forming along the subtropical jet. However, the manner in which precipitation anomalies develop differs between El Niño and La Niña, due to ENSO's influence on the mean jet and baroclinic waves (Shapiro et al. 2001), whose

lifecycle differs under different mean states (Thorncroft et al. 1993). This section examines how predictable wet and dry initializations differ by ENSO phase, given the hypothesized differences in teleconnections in each phase.

320

Splitting dry and wet forecast initializations into periods when Niño3.4 is positive or negative to reflect El Niño or La Niña conditions, without losing any samples, indicates that even when preceding same-signed precipitation anomalies, El Niño and La Niña conditions are associated with different large-scale circulation patterns (c.f., Fig. 11a,c; Fig.11b,d). By construction, there are clear differences in SST and OLR associated with El Niño and La Niña conditions, as well as north Pacific Ψ_{200} anomalies associated with ENSO-like tropical heating (Winkler et al. 2001; Henderson et al. 2020). During La Niña conditions, dry periods include an anticyclonic anomaly over southwest Asia, while during dry El Niño initializations there are cyclonic features north and east of southwest Asia and weak anomalies directly over the region (c.f. Fig. 11a,c). In contrast to the circulation pattern during dry El Niño periods (Fig. 11c), during wet periods, El Niño conditions are associated with an amplified Ψ_{200} pattern, with two high amplitude cyclonic anomalies located over Eurasia (Fig. 11d). Conversely, at the time of initialization during wet La Niña periods, negligible Ψ_{200} anomalies are observed (Fig. 11b).

What distinguishes rainy La Niña or El Niño periods from dry La Niña or El Niño periods? While the heating and SST dipole patterns are consistent for both wet and dry periods of each ENSO phase, there are differences in heating strength and location (c.f. Fig. 11a,b; Fig.11c,d). Dry La Niña initializations include stronger negative SST anomalies and suppressed convection in the central Pacific compared to rainy periods, which instead involve enhanced convection over the maritime continent. Dry El Niño periods include stronger suppressed convection over the Maritime Continent than wet El Niño dates, coinciding with a hint of a wave train emanating from the east Pacific across North America and the north Atlantic. Dry La Niña dates are more common than wet La Niña dates, 84 vs 67 days, while wet El Niño dates are more common than dry El Niño dates, 96 vs 57 days, consistent with past research linking seasonal mean departures of southwest Asian precipitation to ENSO (Hoell et al. 2018a).

Differencing the dry and wet composites between each ENSO phase reveals the common element of suppressed SPCZ convection and cooler central Pacific SSTs during dry periods (Fig. 12). Dry periods during El Niño conditions are associated with warmer SSTs in the east Pacific than wet periods (Fig. 12b), while no such differences in SSTs or OLR are observed in the east Pacific during La Niña conditions. While distinct from one another, the Ψ_{200} patterns during both El Niño and La Niña conditions both place an anomalous anticyclone over southwest Asia during dry events, consistent with suppressed precipitation. The Ψ_{200} patterns during dry versus wet periods differ, with La Niña conditions displaying weak anticyclonic anomalies in the subtropical north Pacific and north Atlantic, and El Niño conditions associated with an upper-level wave train emanating from the eastern tropical Pacific, across the north Atlantic to Europe, potentially linked to the anomaly over southwest Asia. The orientation of such a wave train is consistent with the evolution described by Shaman and Tziperman 2005, who found a northeastward propagating wave train emanating from the east-central Pacific during strong ENSO events,

which ultimately modulated Tibetan snow depth. Thus, while the heating difference between dry and rainy periods is similar regardless of ENSO phase, the impact of the anomalous heating on the circulation is different, but coincidentally yields a reduction in precipitation over southwest Asia. The different circulation responses are consistent with the modified mean states of each ENSO phase, though more work is required to further understand these nuanced relationships, preferably with a larger sample size. Dry baroclinic modelling experiments could be useful in disentangling the role of the basic state and thermal forcing in producing this response.

3.2.3 Relative Risk associated with SPCZ OLR

Given the similar OLR anomalies in the SPCZ region noted during predictable wet and dry forecast initializations (Fig. 10; Fig. 12), a time series of OLR over the region was selected for a final metric to consider related to week 3-4 SFOs. Similar to considering Niño3.4 and RMM, using OLR alone to anticipate periods of elevated skill, the relative risk of a high expected skill date increases significantly as the standard deviation of SPCZ OLR anomalies increases (Fig. 13). The response during negative and positive OLR anomaly values is more symmetric than the risk associated with increasing Niño3.4 threshold, which indicated a greater relative risk increase during El Niño than La Niña conditions (Fig. 7) or comparing the impact of MJO phases 2-3 vs 6-7 (Fig. 9). This symmetry is further supported with the 18-day lagged regression of the southwest Asian precipitation time series with OLR (Fig. S2), although the regression pattern OLR anomalies are weaker than the composite OLR during the SFOs considered in Fig. 10 and 12. SPCZ OLR time series is correlated with the Niño3.4 index at r = -0.25, an indication that the SFOs associated with SPCZ OLR are not redundant with Niño3.4-related SFOs and are therefore contain additional information about SFOs related to tropical variability. As such, the expected skill approach to SFOs benefits from measuring shifts in the likelihood of a forecast of opportunity captured by several distinct indices tracking tropical variability, Niño3.4, RMM and SPCZ OLR, a distinct advantage over using an index that tracks only of these processes (Figs. 3-4).

4 Conclusions

In this study, precipitation SFOs are considered over southwest Asia using LIM expected skill, a metric related to the forecast signal-to-noise ratio that leverages the constructive interference of all signals impacting predictability. Strong El Niño, La Niña and MJO phase 2-3 and 6-7 conditions increase the chances that an SFO occurs. A third tropical heating index, based on anomalous OLR in the SPCZ region, also increases the risk of an SFO (Fig. 13). The correspondence between expected skill and several indices highlights the advantage of using expected skill, in that all of these flavors of tropical heating are registered as high signals. However, there are still SFOs that do not correspond to any one of these indices, since other processes, potentially not tropically-driven, can produce a high signal too. Future work could focus on categorizing all SFOs to examine these potential additional factors.

In addition to the confirmed influence of ENSO and MJO activity on southwest Asian precipitation, anomalous heating along the SPCZ region is a common element among predictable wet and dry initializations and increases the relative risk of an SFO. Heating in this region is also associated with different circulation patterns during El Niño and La Niña conditions (Fig. 12).

385 How these different circulation patterns are related to similar anomalous heating anomalies is currently not well understood, but likely involves the modified tropopause-level waveguide present during each ENSO phase, which modulates the extratropical response to tropical heating (Sardeshmukh and Hoskins 1988; Newman and Sardeshmukh 1998; Shapiro et al. 2001). Dry baroclinic modelling experiments with idealized heating could be used to quantify the contribution of tropical heating over the Indian Ocean and West Pacific in affecting the circulation over southwest Asia on subseasonal timescales.

390 We also note that, while widely used, ENSO indices such as Niño3 or Niño3.4 do not capture the full spectrum of ENSO variability (Penland and Sardeshmukh 1995; Newman et al. 2009; Gehne et al. 2014; Henderson et al. 2020). Future work could employ the dynamical decoupling approach of Henderson et al. (2020) to isolate the ENSO signal and its impact on precipitation SFOs more holistically.

395 The association between forecasts of opportunity and the MJO is less constrained given the higher-frequency nature of the MJO and small sample size once RMM is sorted by phase, but still indicates a role for strong MJO events in phases 2-3 or 6-7 to increase the likelihood of a weeks 3-4 SFO occurring, consistent with prior studies (Cannon et al. 2017; Hoell et al. 2018b). Further suggesting a role for MJO-like heating, predictable heating patterns associated with forecasts of opportunity indicate a role for anomalous convection over the Indian ocean during dry periods, consistent MJO phases 2-3 suppressing southwest

400 Asian precipitation (Fig. 10a). Future work could employ large climate simulation output to enhance sample size and revisit the MJO/expected skill relationship, to the extent the model can reproduce the mean state and MJO itself. Another remaining question that could be addressed more aptly with a larger sample size is how ENSO and the MJO act together to impact SFOs for southwest Asian precipitation events, particularly concerning their magnitude and duration, which was beyond the scope of this study but merits further investigation.

405

Data Availability

The JRA-55 Reanalysis data used in this study is freely available at https://rda.ucar.edu/datasets/ds628.0/, and CHIRPS precipitation is freely available at https://data.chc.ucsb.edu/products/CHIRPS-2.0/global_daily/netcdf/p25/. The RMM index was accessed at no cost from the Australian Bureau of Meteorology here:

410 http://www.bom.gov.au/climate/mjo/graphics/rmm.74toRealtime.txt.

Author Contributions

Melissa L. Breeden wrote code for calculations, produced all figures and wrote the manuscript. John R. Albers provided technical expertise on the LIM and subseasonal forecasting, frequent guidance on computations and figures, and provided edits

to the manuscript. Andrew Hoell secured funding for this project, provided expertise on southwest Asia, frequent guidance on figures, and edits to the manuscript.

Competing Interests

The authors declare no conflict of interest.

420

Acknowledgements

The authors gratefully acknowledge support from the Famine Early Warning Systems Network and helpful suggestions from two anonymous reviewers.

References

425 Agrawala, S., M. Barlow, H. Cullen, and Lyon B.: The drought and humanitarian crisis in central and southwest Asia: A climate perspective. IRI Special Rep. 01–11, 24 pp, 2001.

Albers, J. R. and Newman, M.: A priori identification of skillful extratropical subseasonal forecasts, Geophys. Res. Lett., 46, 12527–12536, https://doi.org/10.1029/2019GL085270, 2019.

430 Albers, J. R. and Newman M.: Subseasonal predictability of the North Atlantic Oscillation, Environmental Research Letters, 16 (4), 044024, 2021.

Barlow, M., Cullen, H. and Lyon B.: Drought in central and southwest Asia: La Niña, the warm pool, and Indian Ocean precipitation. J. Climate, 15, 697–700, https://doi.org/ 10.1175/1520-0442(2002)015,0697:DICASA.2.0.CO;2, 2002.

435

Barlow, M., Wheeler, M., Lyon, B., and Cullen, H.: Modulation of daily precipitation over southwest Asia by the Madden–Julian oscillation. Mon. Wea. Rev., 133, 3579–3594, doi:10.1175/MWR3026.1, 2005.

Barlow, M. A., Cullen, H., Lyon, B. and Wilhelmi, O.: Drought disaster in Asia. Natural Disaster Hotspots Case Studies, M.
440 Arnold et al., Eds., Disaster Risk Management Series, No. 6, World Bank, 1–20, 2006.

Barlow, M., Zaitchik, B., Paz, S., Black, E., Evans, J., and Hoell, A.: A Review of Drought in the Middle East and Southwest Asia, Journal of Climate, 29(23), 8547-8574, 2016.

445   Breeden, M. L., B. T. Hoover, M. Newman, and Vimont, D. J.: Optimal North Pacific Blocking Precursors and Their Deterministic Subseasonal Evolution during Boreal Winter. Mon. Wea. Rev., 148, 739–761, https://doi.org/10.1175/MWR-D-19-0273.1.

Breeden, M. L., Albers, J. R., Butler, A. H., and Newman, M.: The spring minimum in subseasonal 2-meter temperature

450   forecast skill over North America, in production at Monthly Weather Review, 2022.

Cannon, F., L. M. V. Carvalho, C. Jones, A. Hoell, J. Norris, G. N. Kiladis, and Tahir, A. A.: The influence of tropical forcing on extreme winter precipitation in the western Himalaya. Climate Dyn., 48, 1213–1232, https://doi.org/10.1007/s00382-016-3137-0, 2017.

455

de Andrade, F.M., Coelho, C.A.S. and Cavalcanti, I.F.A.: Global precipitation hindcast quality assessment of the Subseasonal to Seasonal (S2S) prediction project models. Clim. Dyn. 52, 5451–5475. https://doi.org/10.1007/s00382-018-4457-z, 2018.

Domeisen, D. I., Garfinkel, C. I., and Butler A. H.: The teleconnection of El Niño Southern Oscillation to the stratosphere.

460   Reviews of Geophysics, 57, 5–47. https://doi.org/10.1029/2018RG000596, 2019.

Famine Early Warning Systems Network: Afghanistan Remote Monitoring Update. 6pp. https://fews.net/sites/default/files/documents/reports/AFGHANISTAN_RMU_April%202022_FINAL.pdf, 2022.

465   Farrell, B. F.: Optimal excitation of neutral Rossby waves. J. Atmos. Sci., 45, 163–172, https://doi.org/10.1175/1520-0469, 1988.

Farrell B F and Ioannou, P. J.: Generalized stability theory. Part I: autonomous operators J. Atmos. Sci. 53, 2025–40, 1996.

470   Funk, C., Peterson, P., Landsfeld, M. Pedreros, D., Verdin, J., Shukla, S., Husak, G., Rowland, J., Harrison, L., Hoell, A., and J. Michaelsen: The climate hazards infrared precipitation with stations—a new environmental record for monitoring extremes. Sci Data, 2, 150066, https://doi.org/10.1038/sdata.2015.66, 2015.

Gehne, M., Kleeman, R. and Trenberth, K. E.: Irregularity and decadal variation in ENSO: a simplified model based on

475   Principal Oscillation Patterns. Clim. Dyn., 43, 3327–3350, https://doi.org/10.1007/s00382-014-2108-6, 2014.

Henderson S. A., Vimont D. J. and Newman, M.: The critical role of non-normality in partitioning tropical and extratropical contributions to PNA growth, *J. Clim.*, **33**, 6273–95, https://doi.org/10.1175/JCLI-D-19-0555.1, 2020.

480   Hoell, A., Barlow, M., and Saini, R.: The leading pattern of intraseasonal and interannual Indian Ocean precipitation variability and its relationship with Asian circulation during the boreal cold season. J. Climate, 25, 7509–7526, doi:10.1175/ JCLI-D-11-00572.1, 2012.

Hoell, A., Barlow, M., and Saini, R.: Intraseasonal and Seasonal-to-Interannual Indian Ocean Convection and Hemispheric
485   Teleconnections, Journal of Climate, 26(22), 8850-8867, 2013.

Hoell, A., C. Funk, and Barlow M.: The regional forcing of Northern Hemisphere drought during recent warm tropical west Pacific Ocean La Niña events. Climate Dyn., 42, 3289–3311, doi:10.1007/s00382-013-1799-4, 2014a.

490   Hoell, A., C. Funk, and Barlow M.: La Niña diversity and northwest Indian Ocean Rim teleconnections. Climate Dyn., 43, 2707–2724, doi:10.1007/s00382-014-2083-y, 2014b.

Hoell, A., C. Funk, and Barlow, M.: The forcing of southwestern Asia teleconnections by low-frequency sea surface temperature variability during boreal winter. J. Climate, 28, 1511–1526, doi:10.1175/JCLI-D-14-00344.1, 2015a.
495
Hoell, A., S. Shukla, M. Barlow, F. Cannon, C. Kelley, and C. Funk: The forcing of monthly precipitation variability over southwest Asia during the boreal cold season. J. Climate, 28, 7038–7056, doi:10.1175/JCLI-D-14-00757.1, 2015b.

Hoell, A., Barlow, M., Cannon, F., and Xu, T.: Oceanic Origins of Historical Southwest Asia Precipitation During the Boreal
500   Cold Season, Journal of Climate, 30(8), 2885-2903, 2017.

Hoell, A., Barlow, M., Xu, T., and T. Zhang: Cold Season Southwest Asia Precipitation Sensitivity to El Niño–Southern Oscillation Events, Journal of Climate, 31(11), 4463-4482, 2018a.

505   Hoell, A., Cannon, F., and Barlow, M.: Middle East and Southwest Asia Daily Precipitation Characteristics Associated with the Madden–Julian Oscillation during Boreal Winter, Journal of Climate, 31(21), 8843-8860, 2018b.

Jin, F. and Hoskins, B. J.: The Direct Response to Tropical Heating in a Baroclinic Atmosphere, 52(3), 307-319, 1995.

510   Johnson, N. C., D. C. Collins, S. B. Feldstein, M. L. L'Heureux, and Riddle, E. E.: Skillful wintertime North American temperature forecasts out to 4 weeks based on the state of ENSO and the MJO. Wea. Forecasting, 29, 23–38, https://doi.org/10.1175/WAF-D-13-00102.1, 2014.

Kalnay, E. and Dalcher, A.: Forecasting Forecast Skill. Monthly Weather Review, 115(2): 349–356. doi: 10.1175/1520-0493(1987)115<0349:ffs>2.0.co;2, 1987.

515

Kobayashi, S., Ota, Y., Harada, Y., Ebita, A., Moriya, M., Onoda, H., Onogi, Kamahori, H., Kobayashi, C., Hirokazu, E., Miyaoka, K., and Takahashi, K.: The JRA-55 reanalysis: General specifications and basic characteristics. Journal of the Meteorological Society of Japan. Ser. II, 93(1), 5–48. https://doi.org/10.2151/jmsj.2015-001, 2015.

520 Lang A. L., Pegion K. and Barnes, E. A.: Introduction to special collection: 'bridging weather and climate: subseasonal- to-seasonal (S2S) prediction'. J. Geophys. Res., 125, e2019JD031833, 2020.

Li S., and Robertson, A.W.: Evaluation of submonthly precipitation forecast skill from global ensemble prediction systems. Mon. Weather. Rev. 143:2871–2889, 2015.

525

Mayer, K. J., and Barnes, E. A.: Subseasonal forecasts of opportunity identified by an explainable neural network. Geophysical Research Letters, 48, e2020GL092092. https://doi. org/10.1029/2020GL092092, 2021.

Mariotti, A., Baggett, C., Barnes, E. A., Becker, E., Butler, A., Collins, D. C., Dirmeyer, P. A., Ferranti, L., Johnson, N. C., 530 Jones, J., Kirtman, B. P., Lang, A. L., Molod, A., Newman, M., Robertson, A. W., Schubert, S., Waliser, D. E., and Albers, J.: Windows of Opportunity for Skillful Forecasts Subseasonal to Seasonal and Beyond, BAMS, 101(5), E608-E625, 2020.

Nazemosadat, M. J., and Ghasemi, A. R.: Quantifying the ENSO-related shifts in the intensity and probability of drought and wet periods in Iran. J. Climate, 17, 4005–4018, https://doi.org/ 10.1175/1520-0442(2004)017,4005:QTESIT.2.0.CO;2, 2004.

535

Nazemosadat, M. J., and Ghaedamini, H.: On the relation- ships between the Madden–Julian oscillation and precipitation variability in southern Iran and the Arabian Peninsula: Atmospheric circulation analysis. J. Climate, 23, 887–904, https://doi.org/10.1175/2009JCLI2141.1, 2010.

540 Newman, M., and Sardeshmukh, P. D.: The impact of the annual cycle on the North Pacific/North American response to remote low-frequency forcing. Journal of the Atmospheric Sciences, 55(8), 1336–1353, 1998.

Newman, M., Sardeshmukh, P. D., Winkler, C. R., and Whitaker, J. S.: A study of subseasonal predictability. Monthly Weather Review, 131(8), 1715–1732. https://doi.org/10.1175//2558.1, 2003.

545

Newman, M., Sardeshmukh, P. D., and Penland, C.: How Important Is Air–Sea Coupling in ENSO and MJO Evolution?, Journal of Climate, 22(11), 2958-2977, 2009.

Pegion, K., Kirtman, B. P., Becker, E., Collins, D. C., LaJoie, E., Burgman, R., Bell, R., DelSole, T., Min, D., Zhu, Y., Li, W., Sinsky, E., Guan, H., Gottschalck, J., Metzger, E. J., Barton, N. P., Achuthavarier, D., Marshak, J., Koster, R. D., Lin, H., Gagnon, N., Bell, M., Tippett, M. K., Robertson, A. W., Sun, S., Benjamin, S. G., Green, B. W., Bleck, R., and Kim, H.: The Subseasonal Experiment (SubX): A Multimodel Subseasonal Prediction Experiment, Bulletin of the American Meteorological Society, 100(10), 2043-2060, 2019.

Penland, C. and Sardeshmukh, P. D.: The optimal growth of tropical sea surface temperature anomalies J. Clim. 8, 1999–2024, 1995.

Riddle, E. E., M. B. Stoner, N. C. Johnson, M. L. L'Heureux, D. C. Collins, and Feldstein, S. B.: The impact of the MJO on clusters of wintertime circulation anomalies over the North American region. Climate Dyn., 40, 1749–1766, https://doi.org/10.1007/s00382-012-1493-y, 2013.

Rodney, M., Lin, H., and Derome, J.: Subseasonal Prediction of Wintertime North American Surface Air Temperature during Strong MJO Events, Monthly Weather Review, 141(8), 2897-2909, 2013.

Sardeshmukh, P. D., and Hoskins, B. J.: The Generation of Global Rotational Flow by Steady Idealized Tropical Divergence, Journal of Atmospheric Sciences, 45(7), 1228-1251, 1988.

Sardeshmukh, P. D., Compo, G. P., and Penland, C.: Changes of Probability Associated with El Niño, Journal of Climate, 13(24), 4268-4286, 2000.

Shapiro, M., Wernli, H., Bond, N., and Langland, R.: The influence of the 1997 – 99 El Niño Southern Oscillation on extratropical baroclinic life cycles over the eastern North Pacific. Quarterly Journal of the Royal Meteorological Society, 127(572), 331–342, 2001.

Shaman, J., and Tziperman E.: The Effect of ENSO on Tibetan Plateau Snow Depth: A Stationary Wave Teleconnection Mechanism and Implications for the South Asian Monsoons, Journal of Climate, 18(12), 2067-2079, 2005.

Schrage, J. M., Vincent D. G. , and Fink A. H.: Modulation of intraseasonal (25–70 day) processes by the superimposed ENSO cycle across the Pacific basin. Meteor. Atmos. Phys., 70, 15–27, 1999.

580

Thorncroft, C. D., Hoskins, B. J., and Wallace, J. M.: Two paradigms of baroclinic-wave life-cycle behaviour. Q. J. R. Meteorol. Soc., 119, 17-56, 1993.

Trenberth, K.E.: The definition of El Niño. Bulletin of the American Meteorological Society, 78(12), 2771–2778,

585   https://doi.org/10.1175/1520-0477(1997)078<2771:TDOENO>2.0.CO;2, 1997.

Trenberth, K.E. and Stepaniak, D.P.: Indices of El Niño evolution. J. Clim. 14(8), 1697–1701, https://doi.org/10.1175/1520-0442(2001)014<1697:LIOENO>2.0.CO;2, 2001.

590   Tseng, K.-C., Barnes, E. A., and Maloney, E. D.: Prediction of the midlatitude response to strong Madden-Julian oscillation events on S2S time scales. Geophysical Research Letters, 45, 463–470. https://doi.org/10.1002/2017GL075734, 2018.

Wheeler, M. C., and Hendon, H. H.: An all-season real-time multivariate MJO index: Development of an index for monitoring and prediction. Mon. Wea. Rev., 132, 1917–1932, https://doi.org/ 10.1175/1520-0493(2004)132,1917:AARMMI.2.0.CO;2,

595   2004.

Winkler, C. R., M. Newman, and Sardeshmukh, P. D.: A linear model of wintertime low-frequency variability. Part I: Formulation and forecast skill. J. Climate, 14, 4474–4494, 2001.

Variable	Domain	% Variance Explained	# EOFs Retained
SST	20°S-20°N, 0-357.5°E	63%	8
OLR	20°S-20°N, 0-357.5°E	54%	23
Ψ_{200}	0-90°N, 0-357.5°E	63%	10
Precip	15-48°N, 40-80°E	70%	10
2mT	15-45°N, 40-90°E	77%	5

600

Table 1. LIM variables that compose the state vector **x**, their domain, and the % variance explained by the retained EOFs. Variables include 200-hPa streamfunction (Ψ_{200}), 2-meter temperature (2mT), sea surface temperature (SST), and outgoing

longwave radiation (OLR). Precipitation (Precip) from the Climate Hazards InfraRed Precipitation with Stations (Funk et al. 2015) Version 2.0 dataset (https://data.chc.ucsb.edu/products/CHIRPS-2.0/) is also used. JRA-55 and CHIRPS are used

605   because they are available in near-realtime (2-3 day lag) and serve as the basis for experimental realtime forecasts, and are available back to at least 1981. Ψ_{200}, SST and OLR anomalies are used on a 2.5 X 2.5 degree horizontal grid, while 2mT and Precip are used on a 0.5 X 0.5 degree grid. The EOFs and PCs retained in **x** are not sensitive to the gridding used (not shown).

Example: LIM forecast with lead time $\tau = 15$ days

$$\mathbf{x}(0) \longrightarrow \quad \hat{\mathbf{x}}(15) = \mathbf{x}(0)\mathbf{G}(15)$$

State Vector Initial conditions

Forecast of State Vector
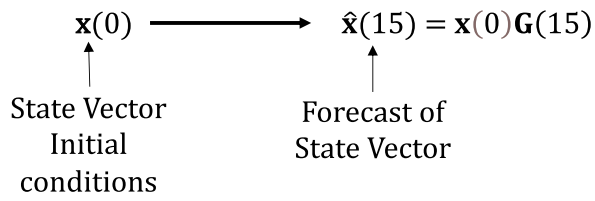
Forecast Propagator: $\mathbf{G}(15) = \exp(\mathbf{L} * 15)$

610   **Figure 1: Schematic of LIM forecast for a lead time of 15 days.**
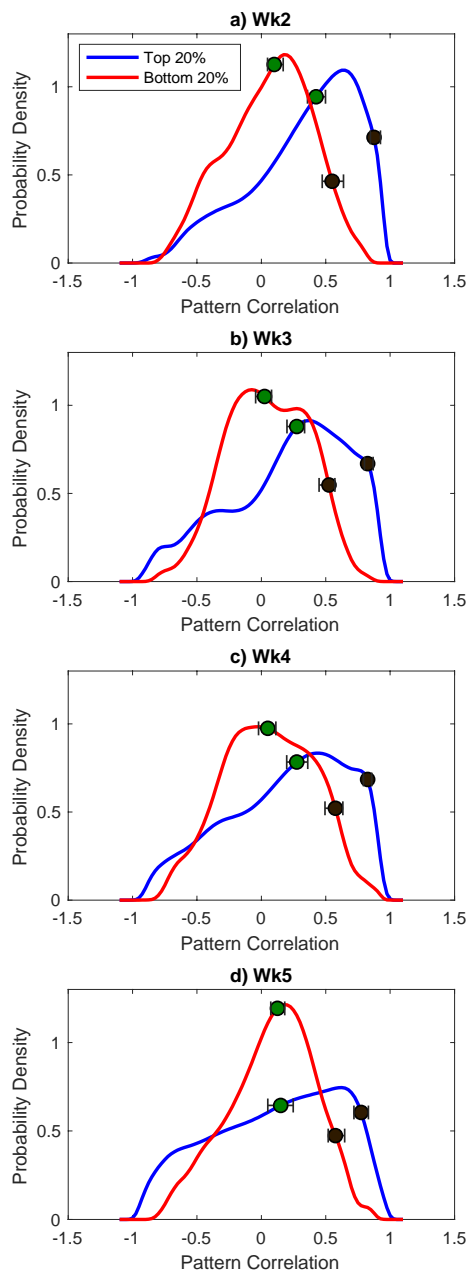
Figure 2: PDFs of actual skill measured by pattern correlation (PCC), for the top 20% and bottom 20% of expected skill dates for weeks of lead times a) two – d) five. The green circles represent the bootstrapped median values, and the black circles represent that bootstrapped 95th percentile values.

615

Weeks 3-4 ACC, Precipitation
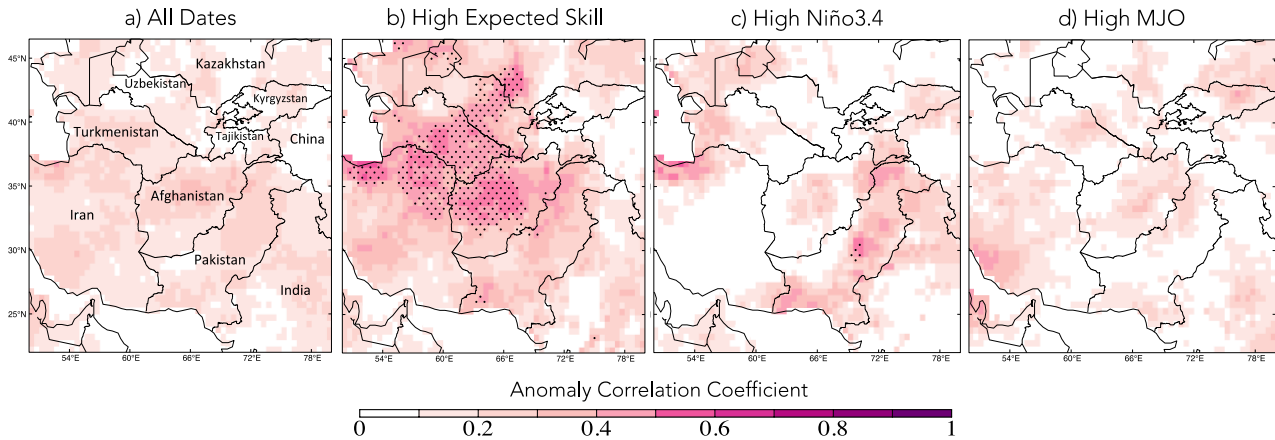
Figure 3: Anomaly correlation coefficient (ACC) for weeks 3-4 forecasts, evaluated from January – March 1982-2020. Panel a) shows ACC for all dates in the record, b) ACC for the 20% of forecasts initialized with the highest expected skill, c) ACC for the 20% with the highest Niño3.4 amplitude, and d) ACC for the 20% with the highest RMM amplitude. The black stippling indicates where the skill of the top 20% of forecasts in each group is statistically significantly different from the skill of the remaining 80% of forecasts at the 95% confidence level, determined nonparametrically with bootstrapping.

Weeks 5-6 ACC, Precipitation
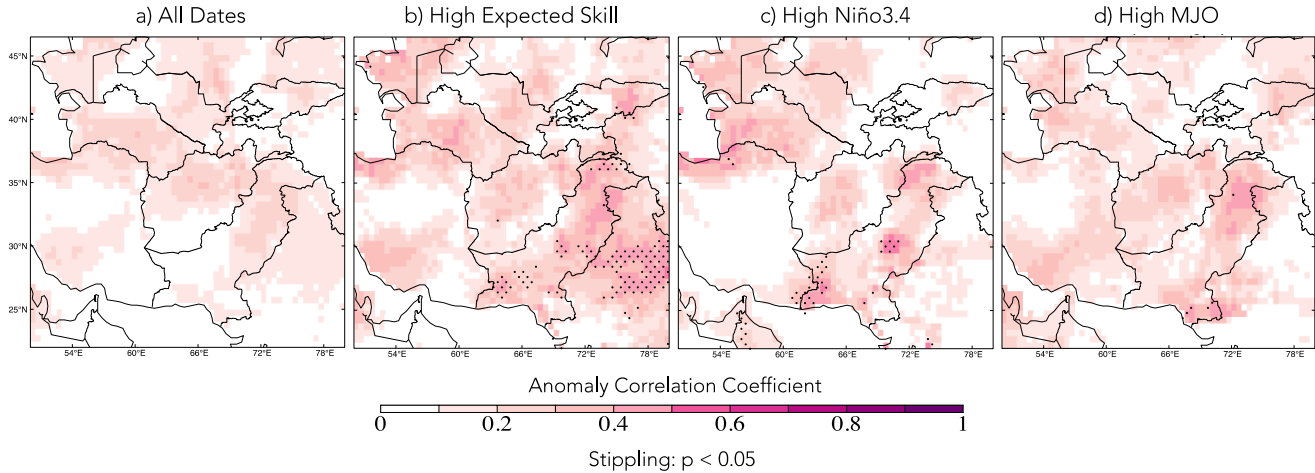
Figure 4: As in Figure 3 but for weeks 5-6 forecasts.
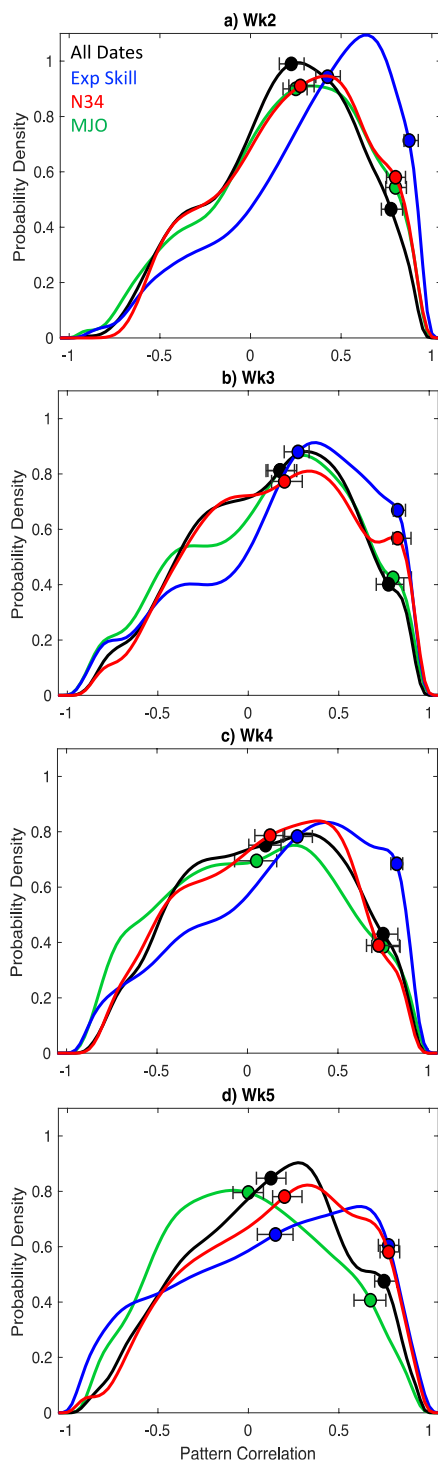
Figure 5: PDFs of precipitation PCC for all forecasts (black lines), the 20% of forecasts with highest expected skill (blue), Niño3.4 (red), and RMM (green) initializations. The bootstrapped confidence intervals for the median and 95th percentile of the distribution are shown with the markers.
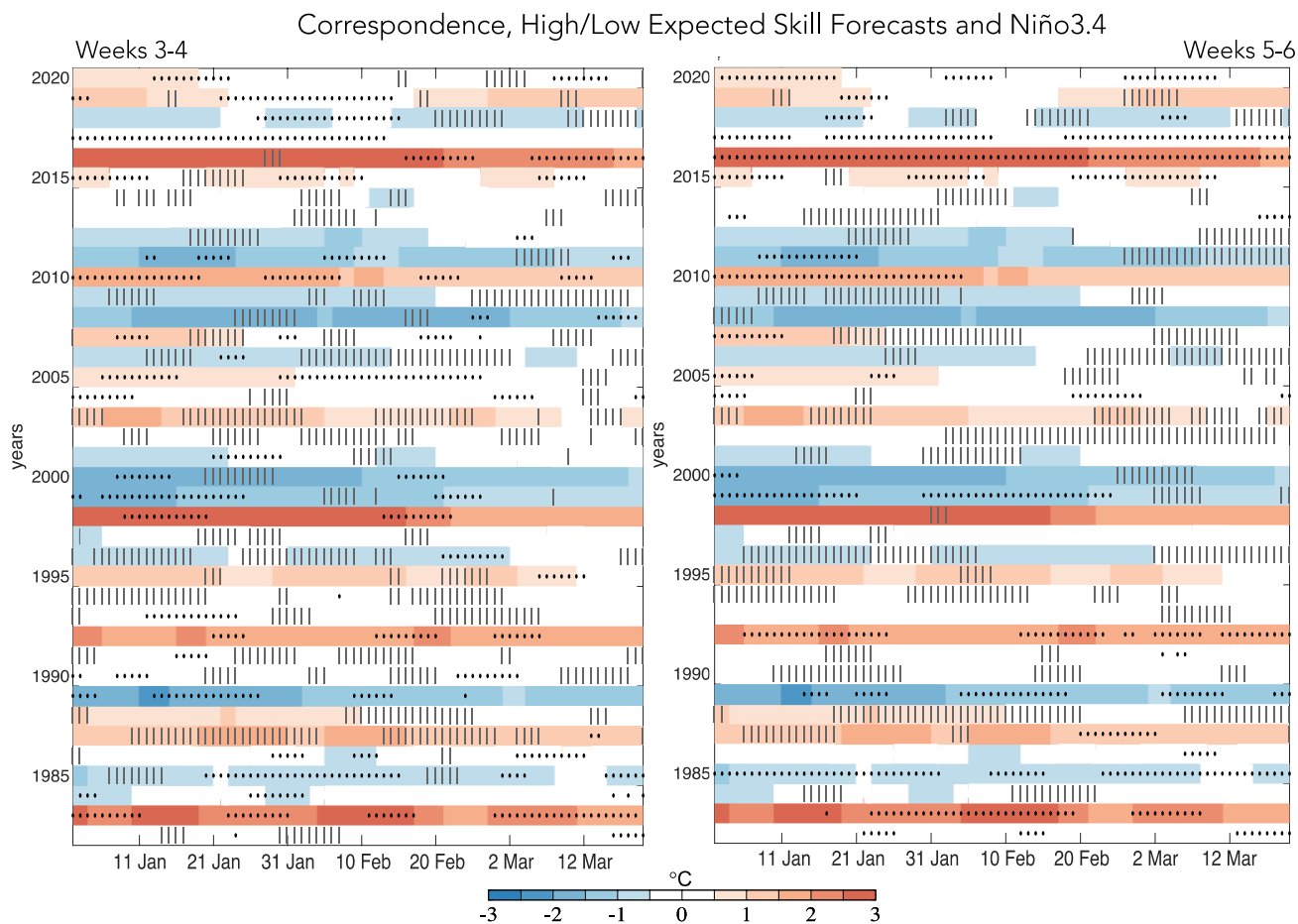
Figure 6: The color shading shows the Niño3.4 index and is the same in both panels. The black dots indicate the top 20% of expected skill forecasts, and the gray vertical lines represent the bottom 20% of expected skill forecasts, for weeks 3-4 forecasts (left) and weeks 5-6 forecasts (right).
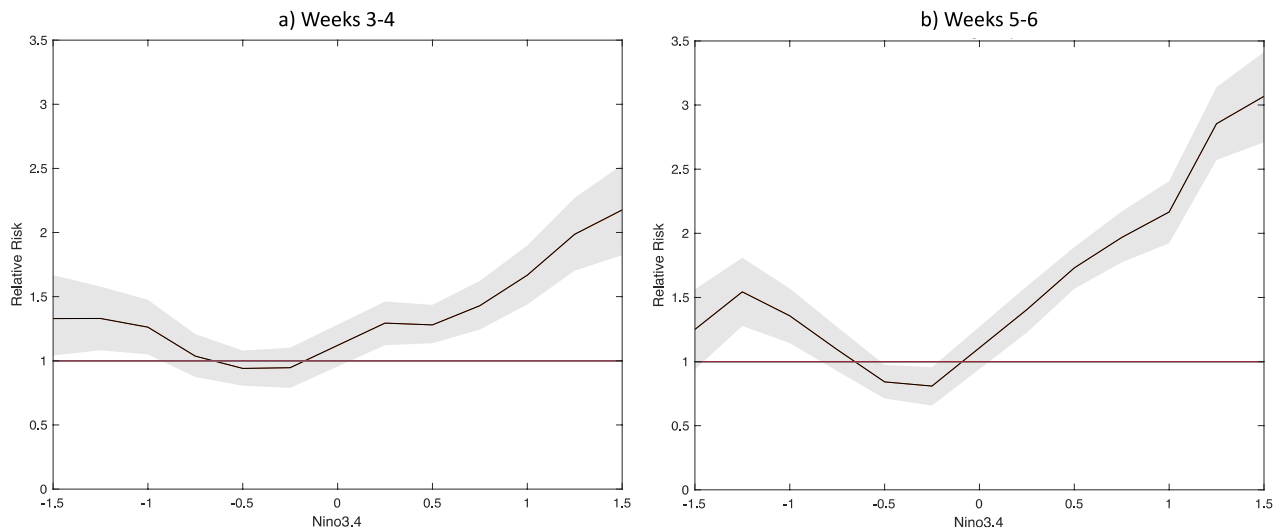
Figure 7: The black line shows the relative risk, relative to the risk on any given day, of an SFO, meaning one of the top 20% of expected skill dates, occurring when the Niño3.4 index is greater than various thresholds, with 95% confidence intervals in gray shading.
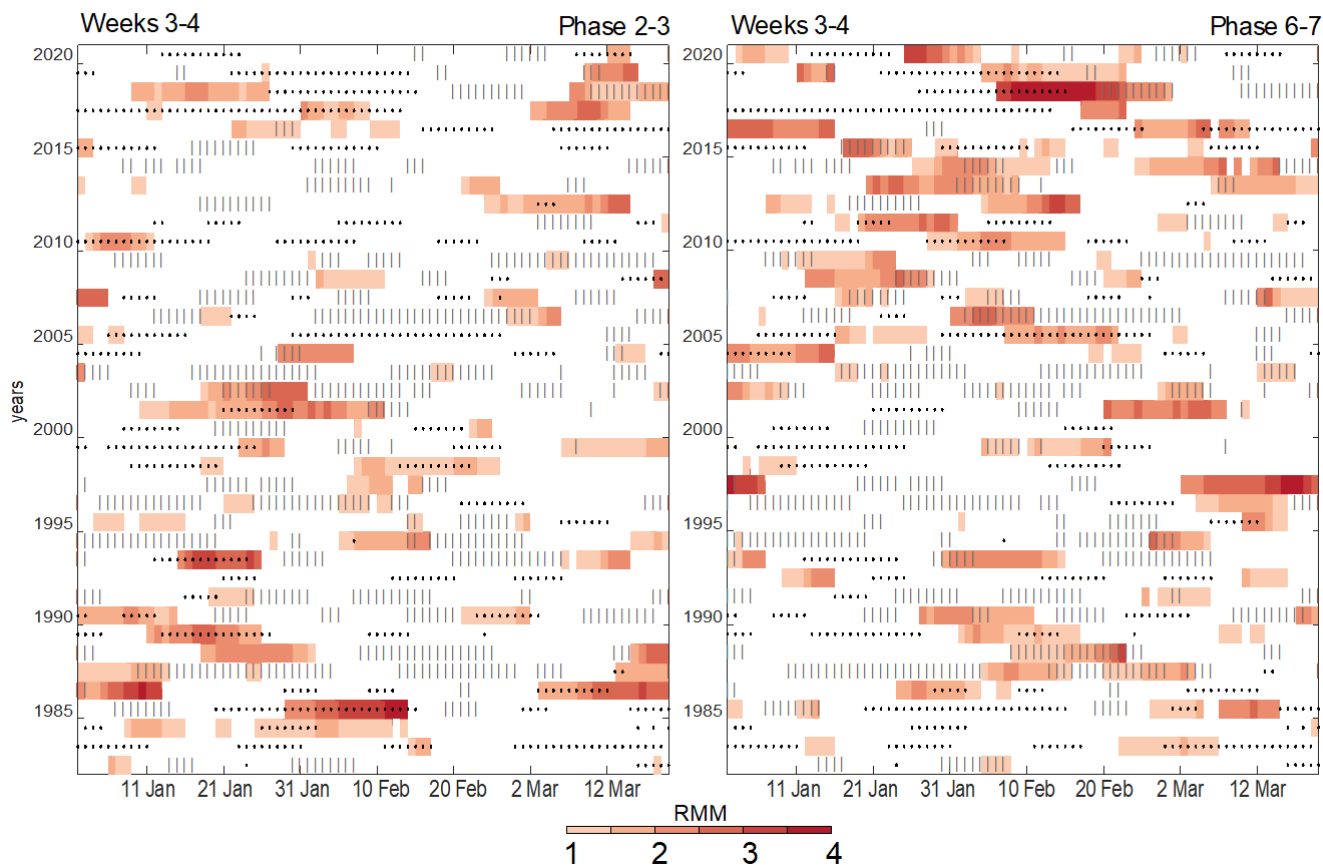
Figure 8: As in Figure 6 but for the amplitude of the RMM index during a) MJO phases 2-3 and b) MJO phases 6-7 and for weeks 3-4 expected skill dates.
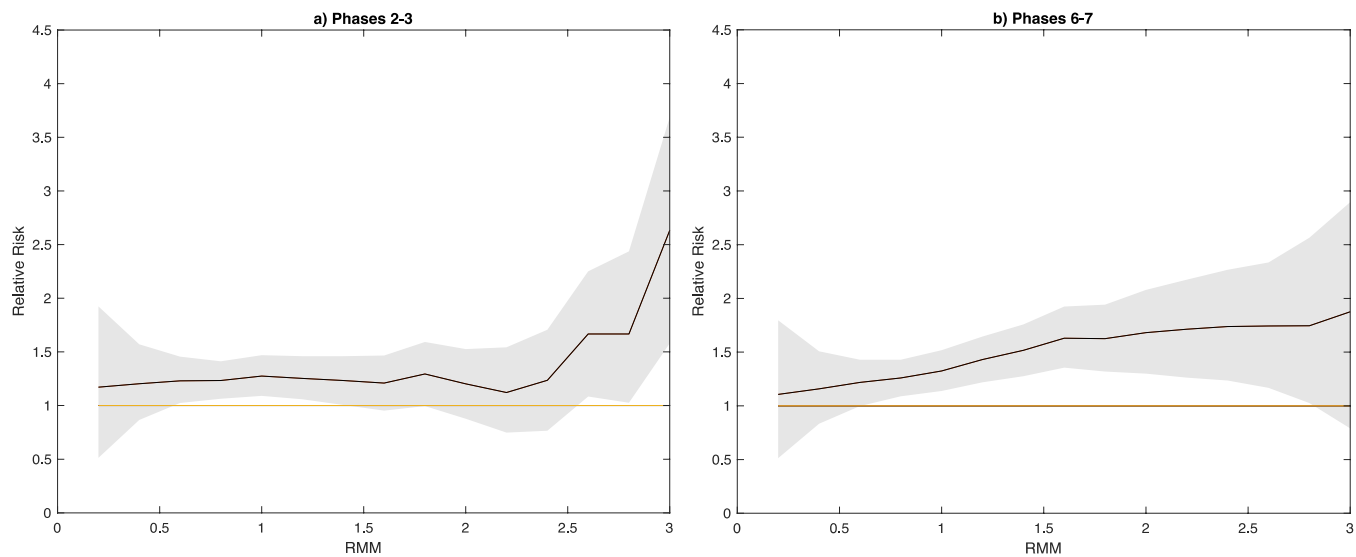
Figure 9: As in Figure 7 but for weeks 3-4 expected skill and for varying RMM amplitude during either MJO phases a) 2-3 or b) 6-7.
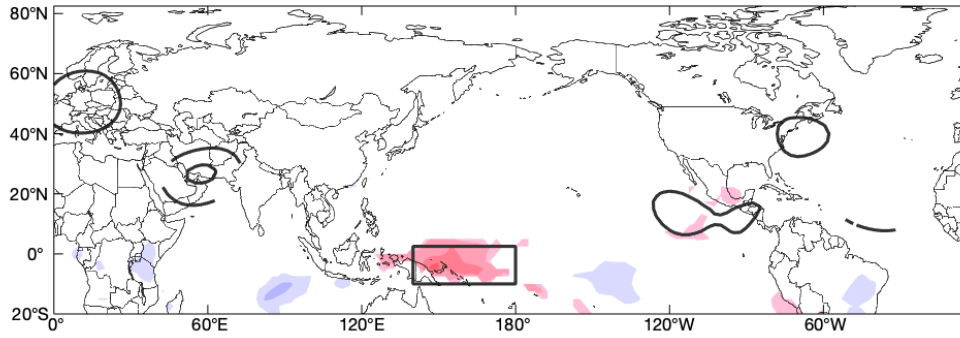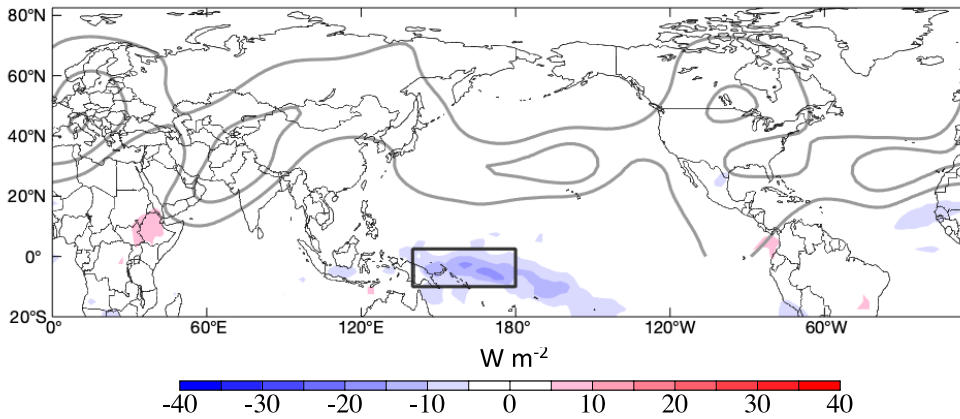
Figure 10: Composite OLR (color shading) and Ψ_{200} (black/gray contours) anomalies, during a) high expected skill initializations verifying on anomalously dry days 18 days later, N = 142 days. Panel b) shows high expected skill initializations verifying on anomalously wet days 18 days later, N = 163.

660

665
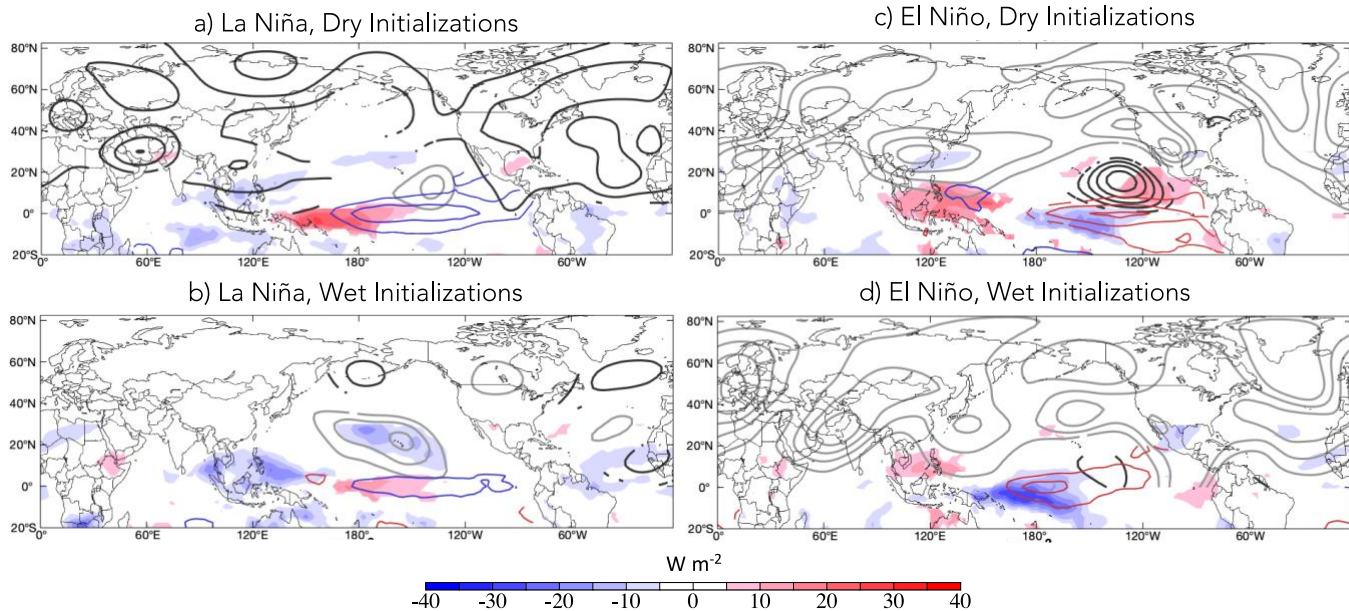
Figure 11: As in Figure 10 but for groups divided by Niño3.4 < 0 ('La Niña') or Niño3.4 > 0 ('El Niño'), and with negative SST anomalies shown in blue contours and positive SST anomalies are shown in red, at a contour interval of 0.5 degrees Celsius.

670
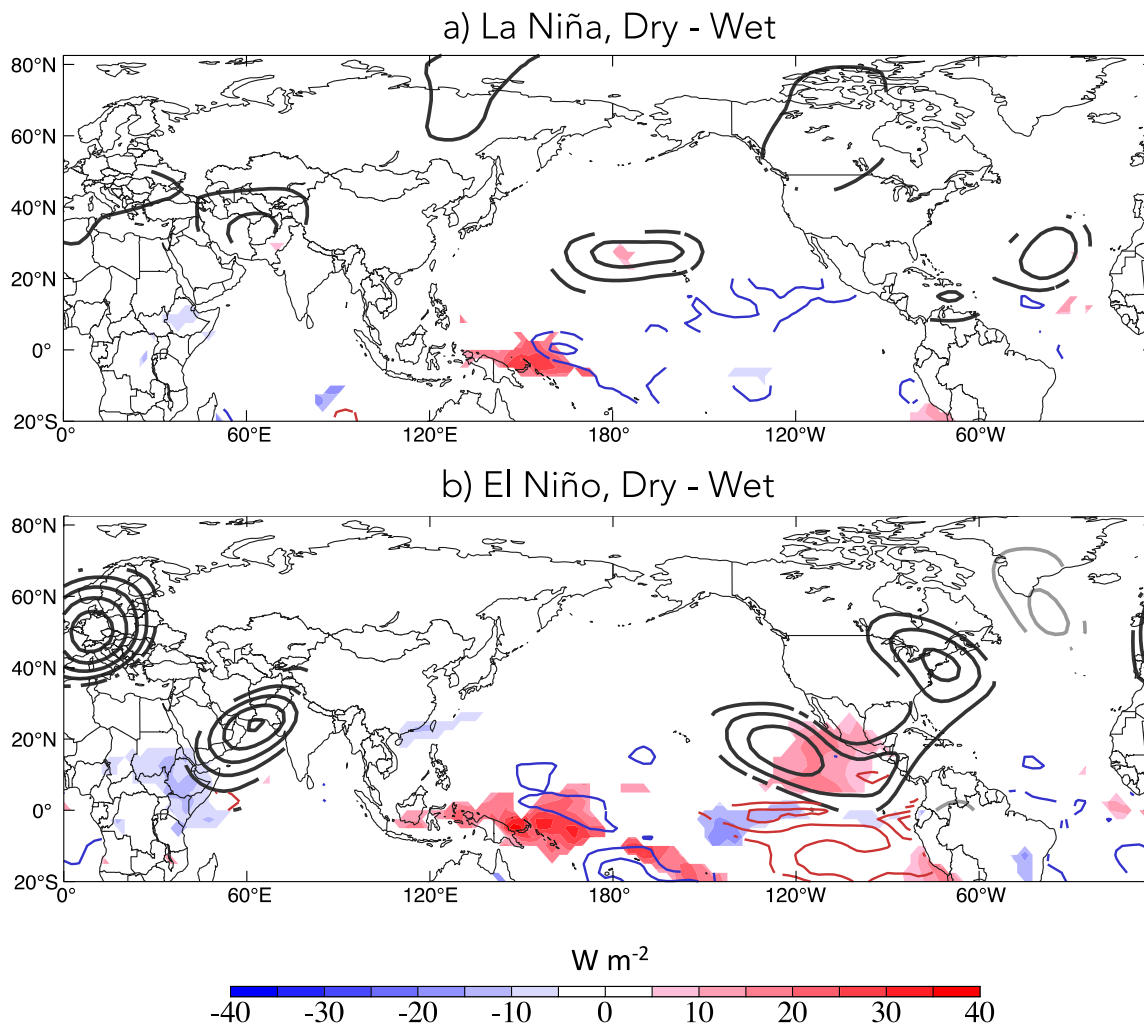
Figure 12: Composite difference, dry – wet, during a) La Niña conditions (Fig. 11a-b) and b) El Niño conditions (Fig. 11c-d).
Plotting conventions are as in Figure 11, except the contour interval for SST anomalies (blue/red contours) is 0.25 degrees
Celsius.
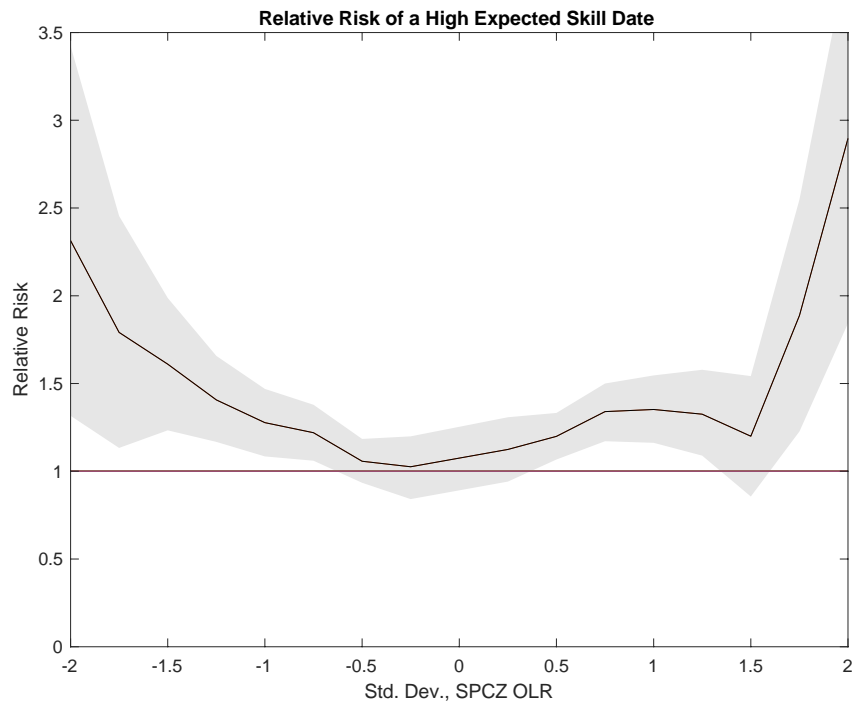
Figure 13: As in Figure 7 but for using the standard deviation of the SPCZ OLR anomaly time series, calculated using the boxed
680 **region in Figure 10 and for weeks 3-4 expected skill.**